JVST B
Journal of Vacuum Science & Technology B

ARTICLE

avs.scitation.org/journal/jvb

Microsphere photolithography using reusable microsphere array mask for low-cost infrared metasurface fabrication

Cite as: J. Vac. Sci. Technol. B 41, 033601 (2023); doi: 10.1116/6.0002557
Submitted: 6 February 2023 · Accepted: 29 March 2023 ·
Published Online: 4 May 2023

Chen Zhu and Edward C. Kinzel[a)]

AFFILIATIONS

Department of Aerospace and Mechanical Engineering, University of Notre Dame, Fitzpatrick Hall, Notre Dame, Indiana 46556

[a)]**Author to whom correspondence should be addressed:** ekinzel@nd.edu

ABSTRACT

Microsphere photolithography (MPL) is an alternative low-cost technique for the large-scale fabrication of periodic structures, such as metasurfaces. This technique utilizes the photonic nanojet generated in the photoresist (PR), by microspheres in near proximity, which are exposed to collimated ultraviolet (UV) flood illumination. In the basic approach, a microsphere array is self-assembled on, or transferred to, the substrate prior to exposure. After exposure, the microspheres are washed away in the development step. The process to recover and clean these microspheres for reuse is complicated. This paper investigates the use of reusable microsphere masks created by fixing the microspheres on a UV transparent support. This is then brought into contact with the photoresist with controlled pressure. There is a trade-off between the quality of the fabricated samples and the wear of the mask determined by the contact pressure. The system is demonstrated using a digital micromirror device (DMD)-based direct-write exposure system to fabricate infrared (IR) metasurfaces. These metasurfaces are characterized and compared to simulation models. Finally, a series of 50 hierarchically patterned IR metasurfaces was fabricated using a single reusable mask. These samples had a <3% coefficient of variance when viewed with a thermal camera. This work shows the potential of mask-based MPL and other contact microlens array-based photolithography techniques for low-cost large-scale fabrication.

I. INTRODUCTION

Metasurfaces consist of a large number of periodic subwavelength elements on the surface and provide electromagnetic properties that can be designed by engineering the geometry and the material of those elements. Metasurfaces have particular advantages relative to thin-film based devices at IR wavelengths because of their reduced thicknesses. The thickness of thin-film devices scales with wavelength and becomes bulky when working at longer wavelengths. Metasurfaces have been proposed for many applications, including imaging,[1,2] sensing,[3] optical cloaking,[4] holograms,[5] energy harnesting,[6,7] and wearable photonics.[8]

Current semiconductor fabrication techniques are capable of patterning metasurfaces. For example, electron beam lithography (EBL) has high flexibility to fabricate arbitrary patterns on planar surfaces. However, they are extremely expensive on a per area basis and challenging to scale up to large areas. Conventional stepper-based photolithography has a lower cost and a higher throughput but sacrifices flexibility. In addition, photolithography highly relies on direct written masks (often EBL/FIB or laser), which are too expensive for metasurface fabrication at a large length scale as well as prototyping applications that need a fast turnaournd.[9] A number of fabrication techniques have been developed to accommodate different fabrication situations. Nanoimprint lithography (NIL)[10] does not need a complicated optical setup but requires extremely high pressure. Step and flash imprint lithography (SFIL)[11] relieves this requirement by using a UV-curable polymer. However, these techniques rely on expensive templates and are challenging to apply to conformal surfaces. Gravure offset printing[12] provides the ability to work with the flexible substrate but still requires an expensive cylinder template. Mask-free fabrication techniques, such as interference lithography[13] and nanosphere lithography (NSL),[14] are potentially lower cost, but they have little control over the element/feature geometries and ability to vary patterns spatially no control over

spatial variation. Also, interference lithography is difficult to apply to conformal surfaces.

Microsphere photolithography (MPL) provides a compromise between cost and flexibility. MPL utilizes self-assembled microsphere arrays as an optical component for focusing rather than a shadow mask used in NSL. Under normal illumination, microspheres generate a narrow intense electromagnetic field at their proximity, which is termed as a photonic nanojet (PNJ).[15] The PNJ has a subwavelength FWHM with a long propagation length up to several wavelengths. The high aspect ratio of PNJ provides MPL the ability to expose PR with a confined feature size. By properly choosing process parameters, MPL is able to fabricate periodic IR metasurfaces, such as perfect absorbers.[16–20] Combining control of the angle of incidence (AOI) and spatial light modulation, the MPL can realize direct writing for IR metasurfaces, which is demonstrated by polarization-dependent structures with hierarchical structures.[21] The low-cost, ease, and potential for a high throughput make MPL attractive for the large-scale fabrication of IR metasurfaces on both planar and conformal surfaces.[22,23]

In the MPL process, a significant part of the cost comes from the microspheres (~$400–$1000 /m^2) for a single-time use plus the operation cost from the repetitive self-assembly process. Recovering the microspheres is possible after the development process; however, cleaning is challenging and the agglomeration/aggregation of the microsphere makes it difficult for the next self-assembly. Another approach is to fix the microspheres on a nonconsumable superstrate as a microsphere mask and bring it into contact with the PR coated on the substrate for exposure. Although not all aim to surface texturing, efforts explored different ways to fix self-assembled microspheres array on the substrate. For example, Sedao *et al.* investigated only using van der Waals forces to fix the microspheres on a glass slide but observed particle detachment during laser structuring.[24] Thermal sintering can be used for mounting microspheres array on a substrate[25–27] but can be challenging because of the high-temperature requirement for materials, such as silica. Ion-beam-induced sintering can reduce the need for high-temperature processing.[28,29] Adhesives can also be used to increase the bonding force between the microspheres and supporting substrates.[30,31] Wu and Whitesides demonstrated the possibility of casting an elastomer around the microspheres for projection lithography,[32] which uses the microspheres as imaging lenses instead of taking advantage of PNJ. In their technique, the gap between the mask and substrate is required to be controlled accurately to achieve good image quality. On the other hand, MPL requires good contact between the microsphere and the substrate because the PNJ generated by the microspheres is a near-field effect in nature. The Talbot pattern has been observed in a photoresist when the mask was positioned 10 μm far from the substrate.[30] Good contact between the mask and substrate can be potentially realized by applying large enough force to the mask/substrate system to minimize the gap distance, which needs to be further investigated.

In this paper, we demonstrate the reusable mask-based MPL technique. The properties of the PNJ generated by the microspheres on the mask are simulated by the frequency domain finite element method (FEM). The contact behavior between the mask and substrate is studied using the Kirchhoff–Love plate bending theory. IR metasurfaces are then fabricated on a flexible substrate using the mask-based MPL with controlled pressure. The digital micromirror device (DMD)-based direct-write exposure system provides spatially modulated exposure. The metasurface performance is characterized by Fourier transform infrared spectroscopy (FTIR) and scanning electron microscopy (SEM). The effect of pressure is summarized from these results, and a trade-off is observed between consistency and mask wear. The results also provide insight into the functional performance of this technique. Finally, 50 IR perfect absorbers are fabricated using a single microsphere mask to demonstrate the reusable mask-based MPL technique.

II. EXPERIMENTAL PROCEDURE

A. Preparation of a reusable microsphere mask

The following procedure is used to prepare the microsphere mask. An optical flat is carefully cleaned with isopropyl alcohol and de-ionized water before it is spin-coated with S1805 PR (Microposit) at 5000 rpm and soft baked for 25 s at 100 °C. Next, 3 μm dry silica microspheres (Nanomicro) are dispensed into butanol with 30 mg/l sodium dodecyl sulfate to make a suspension. The optical flat is submerged in a container of DI water, and the microsphere/butanol suspension is gently dropped onto DI water using a syringe. A capillary force-driven self-assembly of microspheres on the air-water interface draws them to form a hexagonal close-packed (HCP) array. By slowly pulling up the optical flat out of the water, the microsphere array is transferred from the air/water interface to the optical flat and maintains the HCP structure. After transfer, the optical flat is hard-baked at 150 °C for 3 min, 170 °C for 1 min, and then 150 °C for another 3 min to finalize this process. An image of the 2-in. optical flat covered by the polycrystalline microsphere monolayer is shown in Fig. 1(a) with the domain size range from 100 μm to 2 mm. The SEM image of the mask shows both grain boundaries and defects in the HCP microsphere array in Fig. 1(b).

At the hard-bake temperature, reflow and thermal cross-link occur in the PR, resulting in an increased contact area between the PR and the microspheres. The increased contact area between microspheres and PR provides a strong adhesion force. Figure 1(c) shows the SEM image of the HCP microsphere array on the microsphere mask. Figure 1(d) shows a hexagonal depression pattern underlying the PR layer after the microspheres being removed by ultrasonication. This pattern is only observed immediately following the hard-baking process, which indicates that the microspheres are embedded into the PR layer. An embedded depth of $d = 300$ nm could be estimated from the 1.8 μm average diameter of the depression in Fig. 1(d).

B. MPL process and the pattern transfer

Figure 2 shows a schematic illustration of the reusable mask-based MPL process. Initially, S1805 PR is spin-coated onto the substrate at 5000 rpm/s for 60 s, followed by soft baking at 70 °C for 60 s to fix the microspheres. Next, the microsphere mask is placed on top of the substrate and pressure applied on the mask-substrate system during exposure. After exposure, the samples are developed

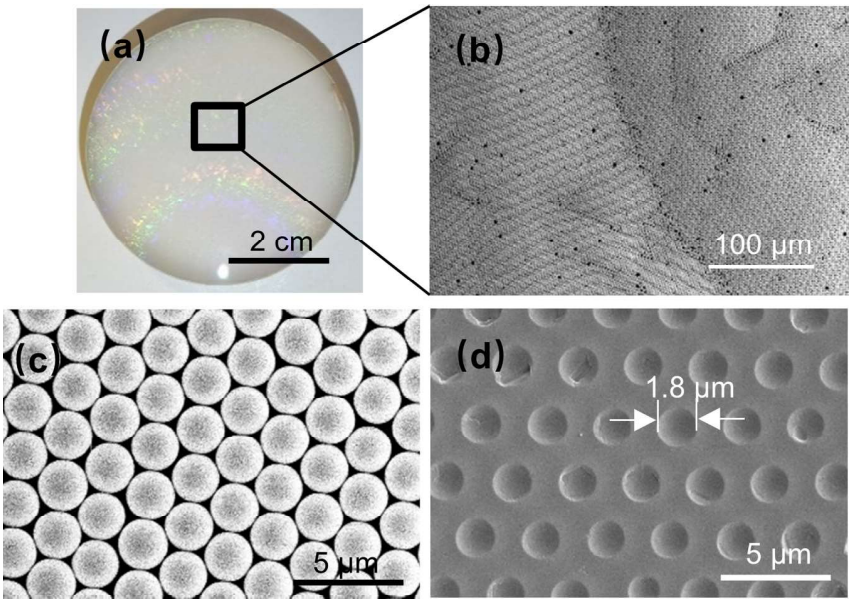

FIG. 1. (a) Microsphere mask based on an optical flat. (b) and (c) SEM images of HCP microspheres on the mask under different magnifications. (d) SEM image of a deformed S1805 photoresist layer after removal of the microspheres.

in MF319 for 30 s. Last, e-beam evaporation is used for metal deposition, and PR is lifted off by Remover PG.

In the exposure step, the microsphere masks are pressed against the substrate to minimize the gap between them. A DMD (DLP6500, Texas Instruments) based projection exposure system is used for dose control and spatial patterning.[20] The micromirrors are pulse-width modulated between tilt angles of +12° and −12° corresponding to the "on" and "off" states, respectively, to produce 8-bit grayscale patterns. Arbitrary digital masks can be used to pattern the sample with a resolution of 1920 × 1080. Figure 3(a) shows the schematic illustration of the system configuration, while (b) shows the practical setup. The DMD is flood illuminated by collimated i-line (365 nm) UV radiation (LS-100X-5CP, Bachur & Associates) at an angle of incidence of 24°. UV radiation incident onto the "on" state mirrors is specularly reflected normally to the DMD surface and imaged onto the substrate by an $f = 100$ mm aspheric lens (AL50100G, Thorlabs) after it is reflected by a beam splitter. The beam reflected from the "off" state micromirror is

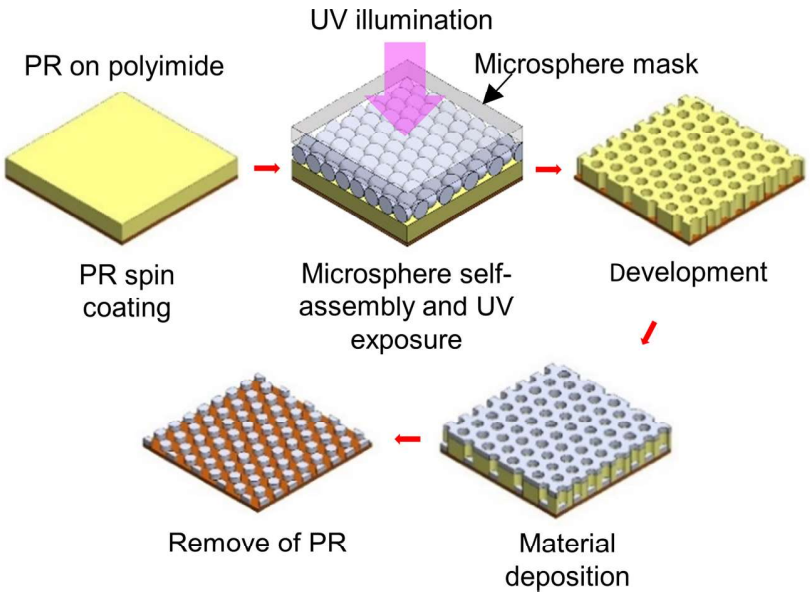

FIG. 2. Step-by-step illustration of a reusable mask-based MPL process.

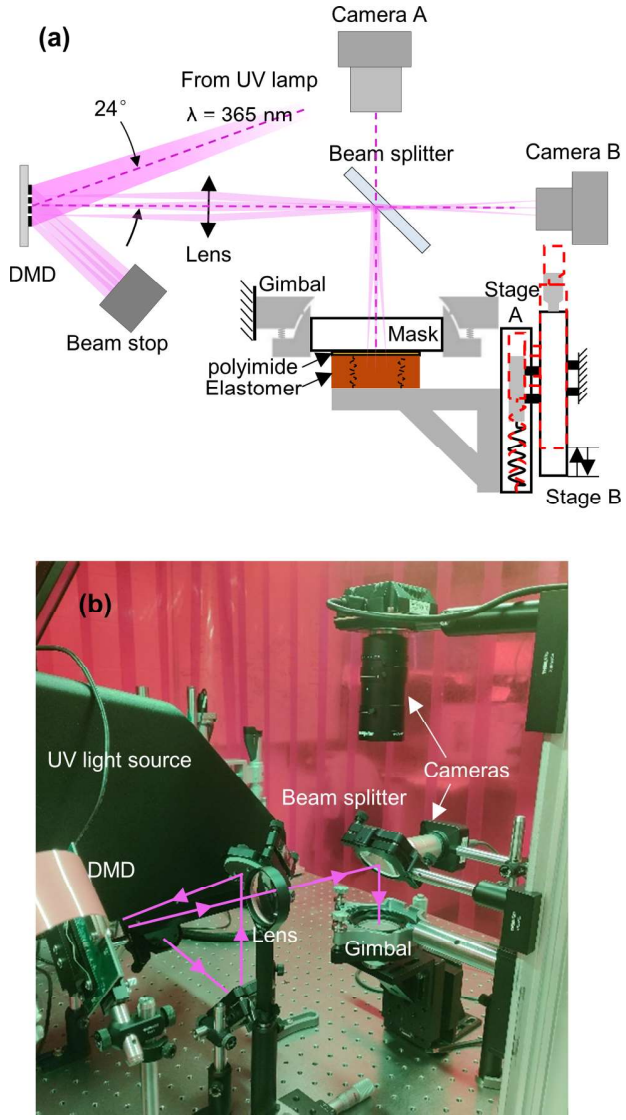

FIG. 3. (a) Exposure system utilizing a DMD digital mask and a gimbal system for applying pressure on a mask-substrate system. (b) Photograph of the experimental setup.

directed to a beam stop. Two digital cameras capture light transmitted through the beam splitter and provide real-time imaging.

The mask is mounted in a gimbal mount (U200-G, Newport) with the microspheres facing down toward the substrate, which is 5 mil polyimide for our experiments. The sample is supported by a 5 mm thick silicone elastomer placed on a right-angle bracket, which is mounted on flipped translation stage A (DDSM100, Thorlabs) without the micrometer drive. The extension springs inside Stage A provide the force required to bring the sample and mask together. Stage A is mounted on a second translation stage B that controls the displacement of the springs inside Stage A. The dashed line in Fig. 3(a) illustrates when Stage B moves upward, and the pressure is increased and vice versa.

The pressure can be precisely adjusted by controlling the displacement of the spring pair mounted inside stage A. Changing among three different sets of springs with spring constants of 44, 557, and 1764 N/m provides a large range of forces. Considering using a $25.4 \times 25.4\ \text{mm}^2$ substrate, the overall pressure can be varied from 0.16 to 17.36 kPa with the 44 N/m springs, 60.2 to 198.15 kPa with the 557 N/m springs, and 91.17 to 452.17 kPa with the 1764 N/m springs.

C. IR metasurface fabrication

In order to make a perfect absorber in the mid-IR range, 150 nm Al followed by 360 nm Ge are deposited on 5 mil polyimide by e-beam evaporation as a substrate. Next, 580 nm S1805 are spin-coated on the substrate and soft baked at 70 °C for 1 min. Then, the substrate is pressed against the microsphere mask for exposure. After exposure, the samples are developed for 30 s followed by lift-off with 100 nm Al. The fabricated IR metasurfaces are characterized using FTIR and SEM.

III. SIMULATION AND MODELING

A. Simulation of PNJ generated by a microsphere mask

Differing from the free-standing microspheres in conventional MPL, the microspheres on the mask are sandwiched by PR on both a superstrate and a substrate. This change of environmental refractive index can affect the properties of the PNJ. Frequency domain FEM simulation (ANSYS HFSS™) shows the electric field of PNJs generated in the photoresist under different conditions. The model of one unit cell has one microsphere on top of the photoresist, and periodic boundary conditions expand the model to an infinity HCP array. Under $\lambda = 365$ nm plane wave excitation, the electric field of PNJ of conventional MPL without a superstrate is shown in Fig. 4(a). Figure 4(b) shows the electric field of PNJ when the microsphere is just in contact with the adhesion layer. The UV radiation is transmitted through the superstrate and the PR prior to the microsphere. The hard-baked S1805 on the microsphere mask (the upper S1805) has a thickness of 510 nm, which is measured using an ellipsometer (VASE, J.A. Woollam), while the soft-baked S1805 on the substrate (the lower S1805) has a thickness of 580 nm. Figure 4(c) shows the more realistic case with the microspheres embedded at a depth of $d = 300$ nm while keeping the other parameters unchanged. The depth is indirectly measured from the SEM image in Fig. 1(d). Figure 4(d) has exactly the same condition as (c) plus a gap $g = 200$ nm between the microsphere and the substrate. It clearly shows the maximum intensity of the E field located inside the photoresist in Figs. 4(a) and 4(b) but located inside the microsphere in Fig. 4(c), in between the microsphere and substrate in Fig. 4(d). The maximum intensity of the E field of the PNJ inside the photoresist in cases (c) and (d) is lower than case (b). Figure 4(e) plots the E^2/E_0^2 field (enhancement factor) distribution along the x axis in the middle plane of the photoresist layer [denoted by a dashed line in (a)–(d)] with varying

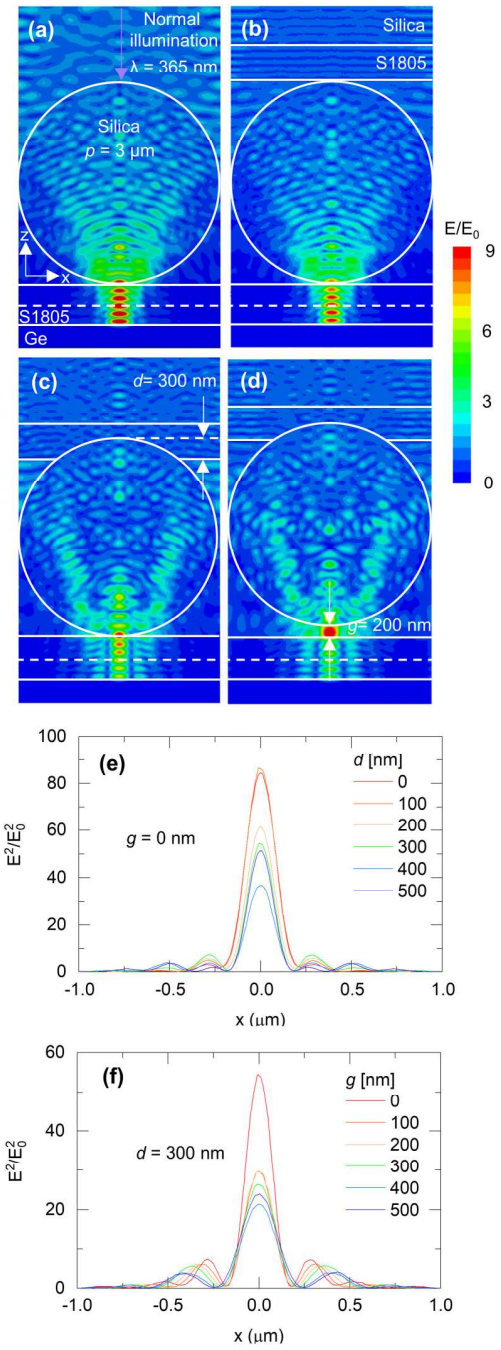

FIG. 4. Electric field of PNJ generated by microspheres ($p = 3\,\mu$m): (a) without a superstrate and in contact with the substrate, (b) resting on the superstrate, (c) embedded to a depth of $d = 300$ nm into the S1805 layer, and (d) embedded depth in a superstrate and separated by a gap of $g = 200$ nm from the substrate photoresist. (e) Electric field distribution in the x direction in the midplane of the S1805 PR layer under the microsphere with varying embedded depth d. (f) Electric field distribution along the x axis with $d = 300$ nm and varying gap g.

embedded depth d. As the microspheres are embedded in the photoresist deeper, the maximum enhancement factor is lowered by half compared to 0 embedded depth and side lobes appear around the PNJ. Figure 4(f) plots the enhancement factor distribution with an embedded depth of $d = 300$ nm for varying gaps g. In this case, the central peak intensity has a significant drop when any gap appears between the microsphere and substrate. In practice, the embedded depth can be controlled through the hard-baking parameters, while the gap distance g has more variations and is more challenging to minimize.

B. Modeling of contact between the mask and the substrate

When the microspheres are fixed on the mask, small variations of the microsphere diameter and surface roughness of the substrate introduce gaps between the PR and microspheres. A solution is to use a compliant substrate, and controllable pressures are used to minimize the gap distance between the microspheres and substrate. A soft supporting material is placed under the substrate to distribute the pressure uniformly. White light interference is used to analyze the contact behavior between the microsphere and the substrate. Figure 5(a) shows a microscope image of a polyimide film when pressure is applied against an optical flat without

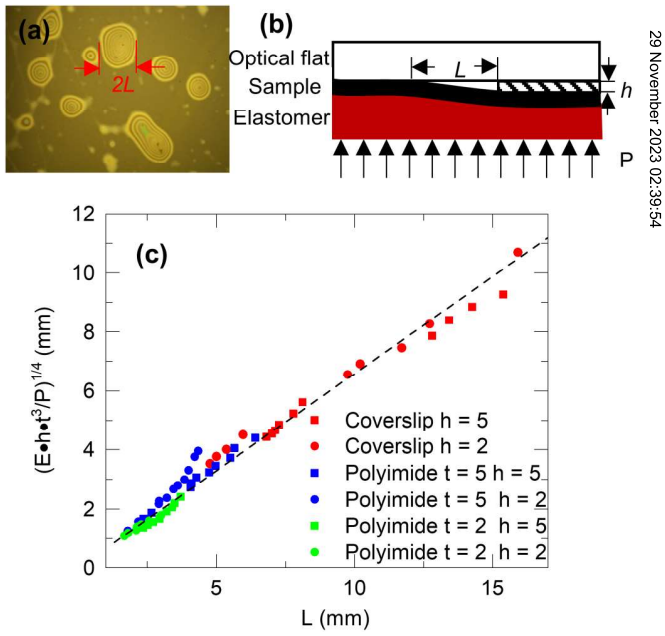

FIG. 5. (a) White light interference pattern generated due to the air gap between the optical flat and substrate. (b) Illustration of the experimental setup relating the affected area with width L to a known step height between the substrate and an optical flat. (c) Relationship between measured affected area width L and the applied pressure with different substrate materials (all units are mil). The dashed line is the theoretical results obtained from the Kirchhoff–Love theory.

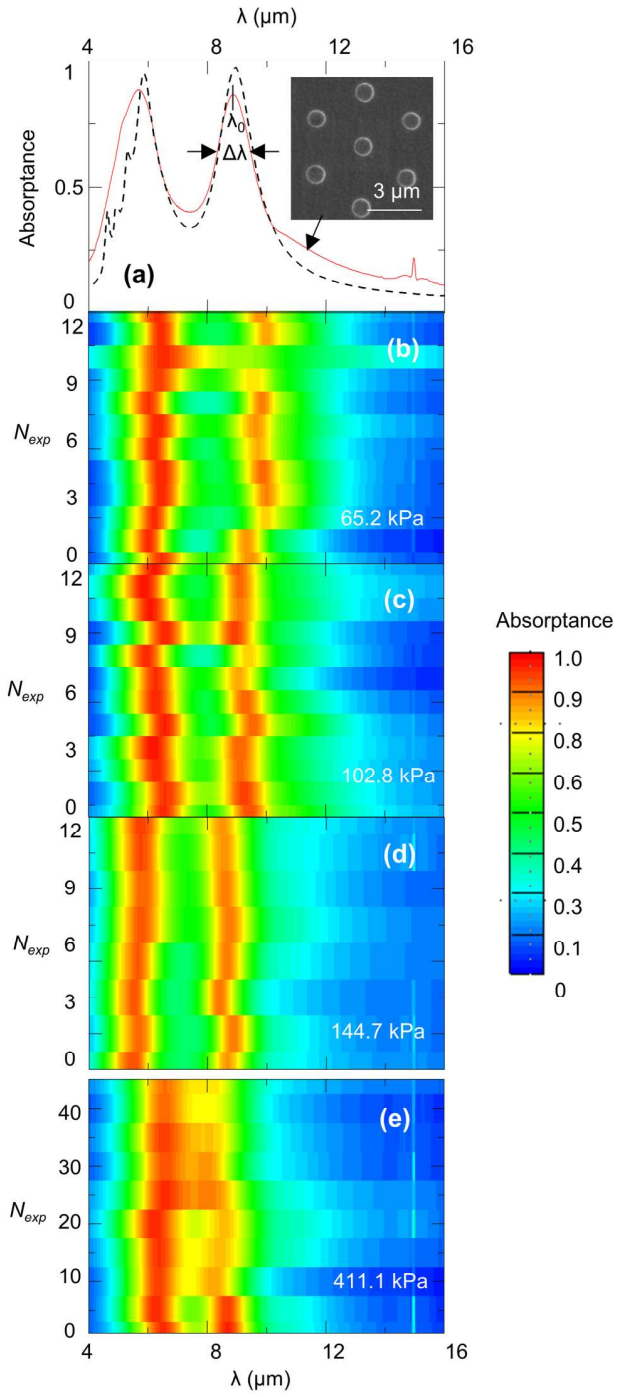

FIG. 6. (a) Measured FTIR absorptance spectra of a fabricated IR perfect absorber compared to simulation results from HFSS™ with an SEM image of disks on a metasurface in the inset. FTIR spectra of an IR perfect absorber with respect to the number of exposure N_{exp} under the pressure of (b) 65.2, (c) 102.8, (d) 144.7, and (e) 411.1 kPa, respectively.

microspheres on top. Thin-film interference caused by gaps in the vicinity of dust and surface defects at the interface can be observed. The area with interference fringes indicates the air gap defined by the defect affected area. The effect of dust or surface defects cannot be eliminated, but the affected area can be minimized by applying enough pressure on the substrate/mask system.

The film deflection can be approximated using the Kirchhoff–Love plate bending theory,[33]

$$y = \left(\frac{Eht^3}{P(1-\nu^2)}\right)^{1/4} = \left(\frac{3}{16}\right)^{1/4} L = kx, \quad (1)$$

where E is Young's modulus of the sample, h is the maximum deflection, equal to the height of the defect, t is the film thickness, P is the pressure applied on the film, and ν is Poisson's ratio. L is the dimension of the affected area with interference patterns. Figure 5(b) is a schematic illustration of the experiment configuration. The equation can be normalized for different materials and different film thicknesses, also experimentally validated by using a known step height and studying the change of the affected area width (denoted by L) with different pressures being applied. A piece of elastomer is used to provide uniform pressure on the sample against an optical flat. The pressure is precisely controlled by using springs and stage displacement. Since introducing point defects with known height is hard in practice, a film with known height is used instead and inserted between the sample and the optical flat to approximate our plate bending model. There is a good agreement between the measured affected area width by applying different pressures on a known step height, and the calculated results from Eq. (1) are shown in Fig. 5(c). A large pressure is required to achieve a smaller affected area, which corresponds to better contact between the sample and mask.

IV. RESULTS AND DISCUSSION

A. Pressure effect and trade-off

In order to study the effects of pressure on practical devices, IR metasurfaces with hexagonal closed packed Al disk arrays over a 1×1 in.^{2} area are fabricated using a microsphere mask on Al/Ge coated polyimide substrates. Pressures of $P = 65.2$, 102.75, 144.71, and 411.1 kPa are used. By adjusting the exposure dose using DMD, the disk diameter D ranges from 900 to 1450 nm with a period $p = 3\,\mu$m, corresponding to the diameter of the microspheres. This produces absorptance peaks between 8 and 10 μm. 8+ identical perfect absorbers are prepared under the same conditions to study the consistency. Figure 6(a) shows a good match between the FTIR absorptance spectra and HFSS™ simulation results (dashed line) on $d = 1\,\mu$m Al disks. The absorptance $A = 1 - R$ is derived from the reflectance, R, measured from FTIR since the ground plane does not permit transmittance through the sample. There are two absorptance peaks in Fig. 6(a) at ~6 μm, and 9 μm corresponds to the Fabry–Perot cavity formed by the Ge layer and the dipole resonance in the Al disks, respectively. The dipole resonance wavelength λ_0 scales with the mean of the disk diameter,[16] while the FWHM $\Delta\lambda$ of the resonance corresponds to the variation of the disk diameter. The inset shows the SEM image of the corresponding Al disks. The effect of pressure on the feature size causes

a variation in the FTIR resonance, as shown in Figs. 6(b)–6(e). Multiple IR perfect absorbers are fabricated using a single microsphere mask for each pressure. As the number of exposure N_{exp} increases, a variation in the absorption peak wavelength has been observed. The standard deviation σ of the resonant wavelength λ_0 is an appropriate indicator of the consistency of the fabrication process. σ is measured to be 283, 182, and 145 nm when $P = 65.2$ kPa, 102.8 kPa, and 144.7 kPa are used, respectively. There is a decreasing trend of σ with increasing pressure. With the other parameters being the same, a variation in the disk diameter results from the gap variance between the mask and substrate. A smaller σ indicates a more uniform gap distance between the mask and substrate under larger pressure. However, as the pressure keeps increasing, fading away of the resonant peak near 9 μm after ~20 exposures is observed in Fig. 6(e) when $P = 411.1$ kPa is used, which results from a gradual microsphere loss.

When the microspheres come into contact with the PR coated substrate, the PR exerts a normal force on the microspheres. After exposure, when the sample is removed from the mask, there is a tensile force that acts to pull the microspheres away from the optical flat. This causes the microspheres to detach from the optical flat. The wear of the mask generally scales with the pressure used. As a consequence, the mask will have a limited lifetime about ~20 times of exposures at 411.1 kPa, which has been illustrated in Fig. 6(e). An optical microscope is used to characterize the mask wear rate under different pressures. Images are taken at the mask before and after each exposure. Figure 7(a) shows an example of the microsphere mask before exposure. Despite individual defects, the HCP microsphere uniformly covers the optical flat. Figure 7(b) is the microscope images captured after 50 times of exposure under $P = 16.1$ kPa with little loss of microspheres. However, when the pressure increases to 158.9 kPa and 411.1 kPa, as shown in Figs. 7(c) and 7(d), the bright areas indicate the surface of the optical flat that is no longer covered by microspheres.

The percentage of microsphere loss could be quantified by measuring the area of the dark region and taking the average from multiple microscope images. The average microsphere losses are plotted in Fig. 7(e). The loss is generally increasing with N_{exp} and the pressure applied to the sample and mask. The mask wear rate is obtained from a linear fit of the microsphere losses as a function of N_{exp} for different pressures. The microsphere coverage (MC) at $N_{exp} = 50$ and the wear rates for different pressures are summarized in Table I.

Figure 8 shows the standard deviation of the resonant wavelength σ and the mask wear with respect to the pressure used in the experiments. Small pressures result in a large variance in resonant wavelengths but have minimal mask wear. Increasing pressure improves metasurface consistency but increases mask wear. If mask wear is limited to 10%, the mask can still be used for over 500 times with a pressure of 158.9 kPa. However, the mask life is reduced to 30 times for 411.1 kPa. There is a trade-off between the number of exposures for the mask and the consistency of the products.

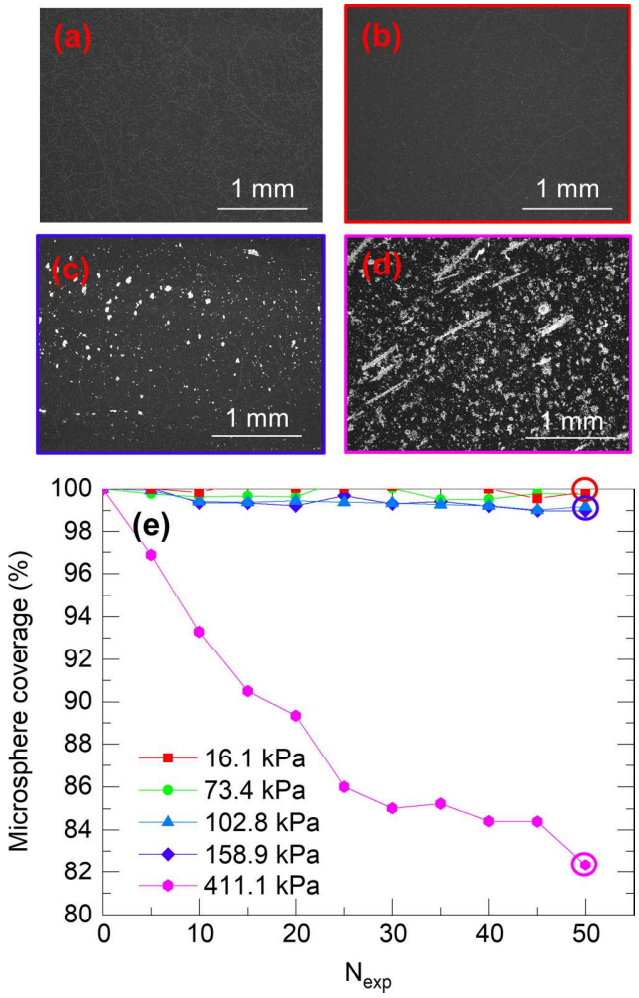

FIG. 7. Microscope images of the microsphere mask (a) immediately following mask preparation, (b) after 50 exposures with 16.1 kPa, (c) after 50 exposures with 158.9 kPa, and (d) after 50 exposures with 411.1 kPa. (e) The percentage of a microsphere coverage change with respect to the number of exposures under different pressures.

B. Demonstration of an IR perfect absorber

Multiple IR perfect absorbers that resonate at different wavelengths are fabricated using mask-based MPL for validation. A

TABLE I. Microsphere coverage measured at $n_{exp} = 50$ and the mask wear rate for different pressures used in the experiment, respectively.

Pressure (kPa)	MC at $N_{exp} = 50$ (%)	Mask wear rate (% per exposure)
16.1	99.85	0.003
73.4	99.73	0.0054
102.8	99.17	0.0166
158.9	98.97	0.0205
411.1	82.34	0.33

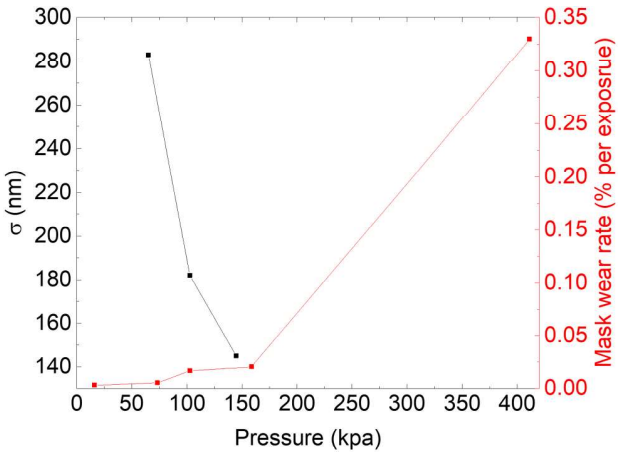

FIG. 8. Pressure induced trade-off between the standard deviation of the resonant wavelength and the mask wear.

significant advantage of using the DMD-based exposure system is that multiple exposure doses can be generated within one single exposure. The exposure dose can be determined by the grayscale value of the DMD digital mask,

$$E = G \cdot I \cdot t/255, \tag{2}$$

where E is the local exposure dose on the sample stage, G is the grayscale value (from 0 to 255) on the DMD, I is the intensity of UV illumination at the sample stage with $G = 255$, and t is the exposure duration. The feature size can be easily controlled by changing the grayscale in the DMD digital mask with the exposure duration fixed. Figure 9(a) displays the FTIR absorptance spectra obtained from six samples of varying disk sizes, which were compared with the simulation results from HFSS™. The SEM images of each sample and their corresponding grayscale values used for disk size control are shown in the inset figure. The FTIR spectra in Fig. 9(a) exhibit two absorption modes, with the first one ranging from 6 to 8 μm being the Fabry–Perot resonance from the dielectric layer. This mode's resonant wavelength is independent of the disk size but primarily determined by the dielectric layer's permittivity and thickness. The second absorption mode is evenly spaced in the range of 8–14 μm, and its wavelength varies with the disk size, indicating that it is a localized plasmonic resonance mode stimulated at the metal disk. This resonance mode depends on both the disk size and dielectric layer properties. To capture images of samples at IR frequencies, we employed an IR camera (Optris Pl640). The camera's acceptable wavelength range (7.9–9.5 μm) is denoted as the shaded area in Fig. 9(a), and we calculated the average absorptance for each spectrum, as shown in Fig. 9(b). The average absorptance varied from 0.2 to 0.65 for different disk sizes. According to Kirchhoff's law of thermal radiation, the absorptivity of a body in a thermodynamic equilibrium is equal to its emissivity. Consequently, the sample with a higher average absorptance appears brighter in the IR camera, while the reverse is true for those with lower average absorptance. By controlling the grayscale of the DMD, we can potentially create a contrast in a thermal image by varying the disk size.

A series of IR absorbers showing the university's mascot is fabricated from a single microsphere mask. 50 IR metasurfaces are fabricated consecutively and imaged by the IR camera (Optris Pl640) at normal incidence. The detail of this imaging setup is

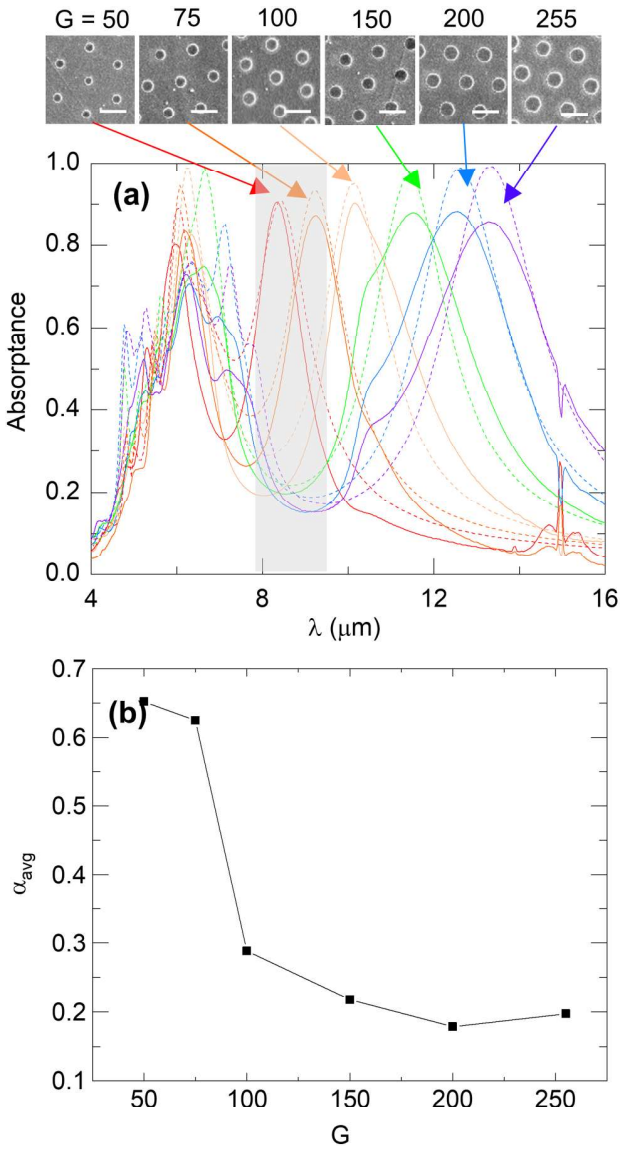

FIG. 9. (a) FTIR absorptance spectra of six samples exposed with different DMD grayscale values of 50, 75, 100,150, 200, and 255 (solid line), compared to simulation results from HFSS™ (dashed line). (b) Average absorptance integrated over the detectable range (7.9–9.5 μm) of the IR camera with respect to different grayscale values used for fabrication.

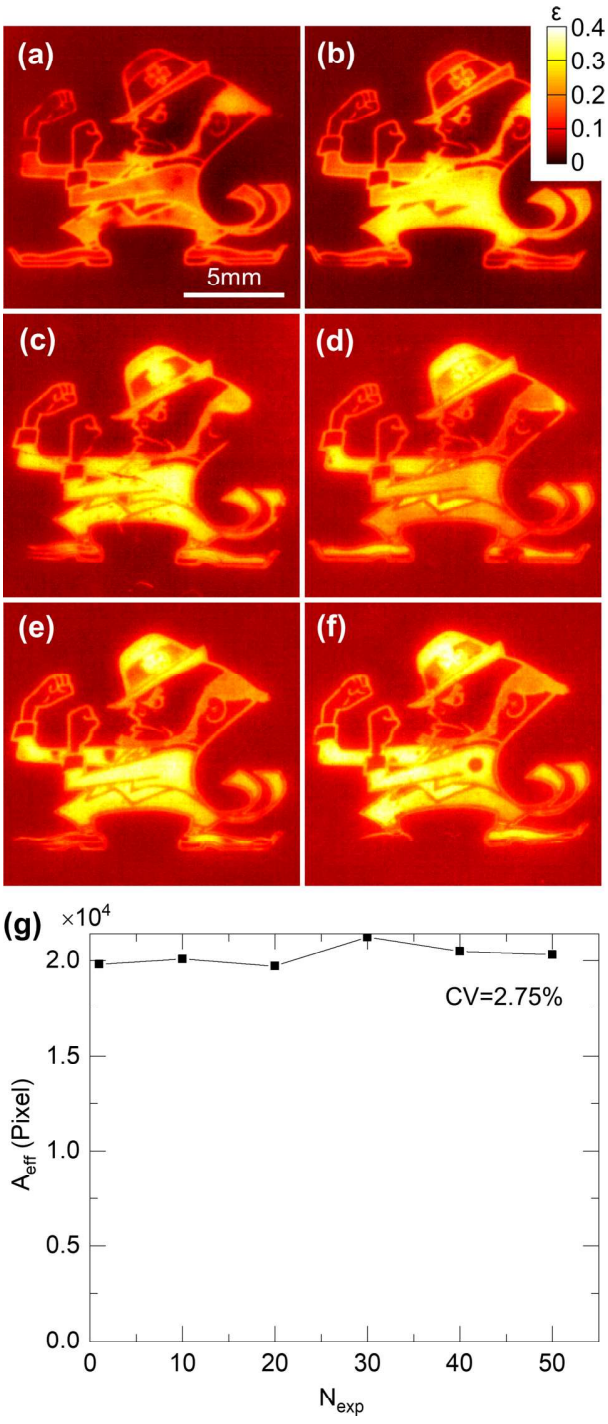

FIG. 10. Thermal images of IR perfect absorbers (showing a university mascot) fabricated from a single microsphere mask. (a) 1st, (b) 10th, (c) 20th, (d) 30th, (e) 40th, and (f) 50th sample fabricated using the mask. (g) Change of the patterned area (measured in pixels) with the number of exposures.

described in our previous paper.[21] Figures 10(a)–10(f) show the emissivity map derived from the thermal image of every tenth sample. Although the background of the image pattern has slightly different emissivity due to the thickness variation in preparing the substrates, the emissivity of all samples is consistent, which indicates little change in the feature size. In addition, the effectively patterned area of each sample can be measured from the thermal image by counting the number of pixels with an emissivity greater than the average emissivity of the whole image. The results are plotted in Fig. 10(g). A coefficient of variation (CV) of an effectively patterned area (A_{eff}) is measured to be 2.75% among these six samples. This illustrates that the fabrication technique is capable of exposing at least 50 IR metasurfaces with stable performance.

V. CONCLUSIONS

This paper investigated a procedure for reusable mask-based MPL. The expense of the MPL technique can be reduced by using the microsphere mask for exposure. Hard-baked S1805 is used as an adhesive agent to bond the microsphere tightly to the optical flat. The strong bonding force provided by the thermal reflow and cross-linking during hard-baking increases the contact area and the bonding strength between the microspheres and optical flat. Simulation proves that the embedded microspheres still have the ability to generate high aspect ratio PNJs during exposure. Springs with different spring constants are used to provide controllable pressure bringing the mask and substrate in good contact for exposure. Maintaining a uniform and minimal gap between the mask and substrate is critical for consistent performance of mask-based MPL. The pressure is proved to be a critical parameter for minimizing the gap distance between the mask and substrate. A trade-off is proved to be associated with pressure between product consistencies and mask wear. When the pressure increases from 65 to 144 kPa, the standard deviation of resonant wavelength decreases from 283 to 145 nm. However, the mask wear increased from 0.005% per exposure to 0.33% per exposure with the pressure increased from 65 to 411 kPa. A pressure of $P = 411$ kPa reduces the maximum number of exposures to ~20 while maintaining the performance of the metasurface. By appropriate choosing a pressure, consistent results can be achieved with a relatively longer mask life. Combined with a DMD direct-write system, 50 IR metasurfaces over 1×1 in.^{2} are fabricated with a CV of 2.75% on a patterned area. Reusable mask MPL has a significant advantage of low-cost fabrication of metasurfaces since it does not require extremely high pressure or expensive masks, as needed in NIL. Additionally, it offers greater flexibility in feature control than NSL. Future work will focus on minimizing the trade-off between mask performance and mask wear. This includes investigating the effect of baking temperature and time on the embedded depth of the microspheres as well as other adhesives that ultimately affect the properties of the PNJ and the robustness of the mask. This will support the fabrication of functional optical and IR metasurfaces.

ACKNOWLEDGMENT

This work was supported by the NSF (No. CMMI-1947391).

AUTHOR DECLARATIONS

Conflict of Interest

The authors have no conflicts to disclose.

Author Contributions

Chen Zhu: Conceptualization (equal); Investigation (lead); Writing – original draft (lead). **Edward C. Kinzel:** Conceptualization (equal); Supervision (lead); Writing – review & editing (lead).

DATA AVAILABILITY

The data that support the findings of this study are available from the corresponding author upon reasonable request.

REFERENCES

[1]M. Khorasaninejad, W. T. Chen, R. C. Devlin, J. Oh, A. Y. Zhu, and F. Capasso, Science **352**, 1190 (2016).
[2]A. Pors, M. G. Nielsen, R. L. Eriksen, and S. I. Bozhevolnyi, Nano Lett. **13**, 829 (2013).
[3]M. L. Tseng, Y. Jahani, A. Leitis, and H. Altug, ACS Photonics **8**, 47 (2021).
[4]J. Valentine, J. Li, T. Zentgraf, G. Bartal, and X. Zhang, Nat. Mater. **8**, 568 (2009).
[5]G. Zheng, H. Mühlenbernd, M. Kenney, G. Li, T. Zentgraf, and S. Zhang, Nat. Nanotechnol. **10**, 308 (2015).
[6]W. Yu, Y. Lu, X. Chen, H. Xu, J. Shao, X. Chen, Y. Sun, J. Hao, and N. Dai, Adv. Opt. Mater. **7**, 1900841 (2019).
[7]A. K. Azad, W. J. M. Kort-Kamp, M. Sykora, N. R. Weisse-Bernstein, T. S. Luk, A. J. Taylor, D. A. R. Dalvit, and H.-T. Chen, Sci. Rep. **6**, 20347 (2016).
[8]Y. Zhang, L. Liang, J. Yang, Y. Feng, B. Zhu, J. Zhao, T. Jiang, B. Jin, and W. Liu, Sci. Rep. **6**, 26875 (2016).
[9]A. Pique and D. B. Chrisey, *Direct-Write Technologies for Rapid Prototyping Applications: Sensors, Electronics, and Integrated Power Sources* (Academic, San Diego, CA, 2002).
[10]S. Y. Chou, P. R. Krauss, and P. J. Renstrom, J. Vac. Sci. Technol. B **14**, 4129 (1996).
[11]D. J. Resnick, S. V. Sreenivasan, and C. G. Willson, Mater. Today **8**, 34 (2005).
[12]M. Pudas, J. Hagberg, and S. Leppävuori, J. Eur. Ceram. Soc. **24**, 2943 (2004).
[13]C. Lu and R. h. Lipson, Laser Photonics Rev. **4**, 568 (2010).
[14]C. L. Haynes and R. P. Van Duyne, J. Phys. Chem. B **105**, 5599 (2001).
[15]H. Mohseni, *Frontiers in Optics 2015*, 18–22 October 2015, San Jose, CA (Optical Society of America, Washington, DC, 2015), Paper FM3B.4.
[16]C. Qu and E. C. Kinzel, Opt. Lett. **41**, 3399 (2016).
[17]C. Qu and E. C. Kinzel, Opt. Express **25**, 12632 (2017).
[18]A. Bonakdar, S. J. Jang, R. L. Brown, M. Rezaei, and H. Mohseni, Proc. SPIE **9170**, 917016 (2014).
[19]W. Wu, D. Dey, O. G. Memis, A. Katsnelson, and H. Mohseni, Nanoscale Res. Lett. **3**, 351 (2008).
[20]H. Zheng, Y. Zhou, C. F. Ugwu, A. Du, I. I. Kravchenko, and J. G. Valentine, ACS Photonics **8**, 1824 (2021).
[21]C. Zhu, C. Qu, and E. C. Kinzel, Appl. Opt. **60**, 7122 (2021).
[22]L. Berthod, O. Shavdina, F. Vocanson, M. Langlet, O. Dellea, C. Veillas, S. Reynaud, I. Verrier, and Y. Jourlin, Microelectron. Eng. **177**, 46 (2017).
[23]I.-T. Chen, E. Schappell, X. Zhang, and C.-H. Chang, Microsyst. Nanoeng. **6**, 1 (2020).
[24]X. Sedao, T. J.-Y. Derrien, G. R. B. E. Romer, B. Pathiraj, and A. J. Huis in 't Veld, J. Appl. Phys. **112**, 103111 (2012).
[25]T. Yamasaki and T. Tsutsui, Jpn. J. Appl. Phys. **38**, 5916 (1999).
[26]P.-S. Tsai, Y.-M. Yang, and Y.-L. Lee, Nanotechnology **18**, 465604 (2007).
[27]P. Kumnorkaew, Y.-K. Ee, N. Tansu, and J. F. Gilchrist, Langmuir **24**, 12150 (2008).
[28]D. Kraus, J. K. N. Lindner, and B. Stritzker, Nucl. Instrum. Methods Phys. Res. B **257**, 455 (2007).
[29]J. K. N. Lindner, B. Gehl, and B. Stritzker, Nucl. Instrum. Methods Phys. Res. B **242**, 167 (2006).
[30]C. Qu and E. C. Kinzel, *International Manufacturing Science and Engineering Conference*, 18–22 June 2018, College Station, TX (American Society of Mechanical Engineers, New York, 2018), Vol. 51388.
[31]C. O'Connell, R. J. Sherlock, and T. J. Glynn, Opt. Eng. **49**, 014201 (2010).
[32]M.-H. Wu and G. M. Whitesides, Appl. Phys. Lett. **78**, 2273 (2001).
[33]J. N. Reddy, *Theory and Analysis of Elastic Plates and Shells*, 2nd ed. (CRC, Boca Raton, FL, 2006).